TU Delft

Delft University of Technology

On the inherent correlation between the fluidization and flow properties of cohesive powders

van der Sande, P. Christian; Wu, Kaiqiao; Kamphorst, Rens; Wagner, Evert C.; Meesters, Gabrie M.H.; van Ommen, J. Ruud

DOI
10.1002/aic.18706

Publication date
2024

Document Version
Final published version

Published in
AIChE Journal

Citation (APA)
van der Sande, P. C., Wu, K., Kamphorst, R., Wagner, E. C., Meesters, G. M. H., & van Ommen, J. R. (2024). On the inherent correlation between the fluidization and flow properties of cohesive powders. *AIChE Journal*. https://doi.org/10.1002/aic.18706

Important note
To cite this publication, please use the final published version (if applicable).
Please check the document version above.

Copyright
Other than for strictly personal use, it is not permitted to download, forward or distribute the text or part of it, without the consent of the author(s) and/or copyright holder(s), unless the work is under an open content license such as Creative Commons.

Takedown policy
Please contact us and provide details if you believe this document breaches copyrights.
We will remove access to the work immediately and investigate your claim.

This work is downloaded from Delft University of Technology.
For technical reasons the number of authors shown on this cover page is limited to a maximum of 10.

Check for updates

Received: 4 June 2024 | Revised: 17 September 2024 | Accepted: 10 December 2024

DOI: 10.1002/aic.18706

RESEARCH ARTICLE

Particle Technology

AIChE JOURNAL

On the inherent correlation between the fluidization and flow properties of cohesive powders

P. Christian van der Sande[1] | Kaiqiao Wu[1,2,3] | Rens Kamphorst[1] | Evert C. Wagner[1] | Gabrie M. H. Meesters[1] | J. Ruud van Ommen[1]

[1]Department of Chemical Engineering, Delft University of Technology, Delft, The Netherlands

[2]School of Chemical Engineering and Light Industry, Guangdong University of Technology, Guangzhou, China

[3]Guangdong Provincial Laboratory of Chemistry and Fine Chemical Engineering Jieyang Center, Jieyang, China

Correspondence
Kaiqiao Wu, School of Chemical Engineering and Light Industry, Guangdong University of Technology, Guangzhou 510006, China.
Email: kaiqiao.wu@gdut.edu.cn

J. Ruud van Ommen, Department of Chemical Engineering, Delft University of Technology, Delft 2628 HZ, The Netherlands.
Email: j.r.vanommen@tudelft.nl

Funding information
Nederlandse Organisatie voor Wetenschappelijk Onderzoek, Grant/Award Number: 741.019.202; Netherlands Ministry of Economic Affairs and Climate Policy, Grant/Award Number: 2020.023.A.TUD.1; National Natural Science Foundation of China, Grant/Award Number: 52406181

Abstract

In this study, we investigate the correlation between fluidization behavior and flow properties of 10 commercially available cohesive powders through fluidization and rotating drum experiments. The rotating drum was operated at high speeds to aerate the powder, creating flow fields and stress conditions comparable to those in gas–solid fluidized beds. We introduce a fluidization quality index (FQI) computed from X-ray imaging, which addresses the limitations of conventional analyses for assessing fluidization quality of cohesive powders. By analyzing flow patterns, the FQI integrates gas holdup and its temporal variation, providing a reliable measure of fluidization quality. The findings establish a positive correlation between flowability and fluidization quality, demonstrating how flowability measurements can predict the effectiveness of mechanical vibration in enhancing fluidization characteristics. These results suggest that fast, user-friendly flowability assessments in a rotating drum can effectively predict fluidization potential, contributing to process optimization and advancing fluidization studies for cohesive powders.

KEYWORDS
fluidized bed, Geldart C, powder flow, rotating drum, X-ray imaging

1 | INTRODUCTION

Solid particles are used in fields including catalysis, pharmaceutical, chemical, and environmental industries. In recent years, a gradual shift has taken place towards the use of powders with smaller particle sizes due to the beneficial properties of their high surface-to-volume ratio, for example, in the fields of medicine,[1] catalysis,[2] and composite development.[3] Therefore, handling such solids is becoming a more important component of many industrial processes. The smaller particle sizes introduce complications, however, as the attractive van der Waals forces start dominating over other forces at smaller particle sizes, making the powders cohesive and impeding flow and aeration.[4] Challenges associated with this cohesiveness limit the applicability of conventional processing methods like gas–solid fluidization.

Gas–solid fluidization is realized by passing a gas upward through a bed of settled particles to suspend them in a fluid-like state, which results in homogeneous solids mixing and efficient heat and mass transfer between the two phases.[5] In the context of fluidization, several classification systems exist in which cohesiveness plays an essential role, most prominently the Geldart classification and Bond number.[6] The use of the Geldart classification is widespread in particular, as its prediction of fluidization behavior is solely based on particle

This is an open access article under the terms of the Creative Commons Attribution License, which permits use, distribution and reproduction in any medium, provided the original work is properly cited.
© 2024 The Author(s). *AIChE Journal* published by Wiley Periodicals LLC on behalf of American Institute of Chemical Engineers.

size and density, which are typically easy to obtain.[7] Generally, coarse powders, such as Geldart group A and B, can be well fluidized. Cohesive powders, such as Geldart group A/C and C; however, tend to form agglomerates such that, upon fluidization, both primary particles and particle agglomerates are present in the bed, while the fundamental description of agglomerate formation and breakup—either it is force or energy based—is largely debatable, making it challenging to predict fluidization behavior.[6] Additionally, agglomerates are fragile by nature, making it difficult to assess their properties.[8] Associated with this complexity, Geldart group A/C powders within the Geldart classification, which are typically recognized as cohesive (or mildly cohesive), have been observed to occasionally form agglomerates as well.[9,10] It should also be pointed out that the boundary between type A and C powders is poorly defined, in part due to the fact that density and primary particle size are not the sole parameters determining powder behavior.

Adding to the complexity of predicting fluidization behavior based on particle properties is that cohesive powders typically do not fluidize upon utilizing unassisted fluidization techniques, showing channeling and plugging instead.[7] The latter challenges the design and operation of conventional fluidized beds of cohesive powders, thereby limiting practical applications. Over time, methods have been developed that aid the fluidization of cohesive powders by introducing an additional source of energy to the bed that disrupts channeling.[11] These assistance methods include mechanical stirring,[12,13] gas pulsation,[14,15] acoustic waves,[16,17] and mechanical vibration.[18,19] In particular, mechanical vibration has been recognized as an effective method of aiding the fluidization behavior of cohesive powders and, therefore, readily finds practical applications. However, despite the significant progress in aiding the fluidization of cohesive powders, there is still a missing ability to predict whether a particular fine powder will be fluidized with or without the implementation of an assistance method, and which assistance method is optimal and effective remains a challenging task. Moreover, carrying out fluidization experiments is time-consuming and requires substantial infrastructure to regulate gas supply and ensure safe gas outlet handling, particularly when dealing with fine particles that are highly prone to entrainment. For practical applications, direct visualization of fluidization behavior is challenging. Therefore, the assessment largely relies on indirect measurements, such as pressure drop and bed expansion. Furthermore, the observed phenomena can be scale-dependent and are susceptible to initial conditions, which are, in turn, influenced by user-dependent factors. Consequently, there is a pressing need for fast, user-friendly, and user-independent powder flow testing methods.

For cohesive powder, the degree of cohesion significantly affects flowability, therefore, a wide array of powder flow testing methods has been developed to characterize the flow properties of powders.[20–24] For mildly cohesive powders, quantitative indicators, including angle of repose,[25] angle of avalanche,[26] powder discharge flow,[27] torques in aerated powder bed,[28] were measured to assist the interpretation of powder cohesion. For adequate characterization in relation to a unit operation, the flow field and stress state of the powder should be comparable in the powder flow tester and the respective unit operation.[21,29] In a fluidized bed, the powder bed can be considered to be in a highly dispersed and low consolidation state. Rotating drums have been widely used to characterize the flowability of powders in the dynamic flowing regime in a state of low consolidation.[26,30–34] The rotating drum powder characterization instrument comprises a cylinder typically half-filled with powder that is rotated around its axis at desired rotation speed. Interestingly, several studies have shown that a cohesive powder bed can transition from a quasi-periodic avalanche mode to a fluidized mode as the rotation speed increases.[35–39] At low speeds, the powders initially undergo periodic avalanches. These avalanches result in mixing with the surrounding gas, which can lead to partial fluidization by entraining gas. As the rotation speed increases, the time it takes for the entrained gas to be evacuated becomes comparable to the interval between avalanches. This leads to the establishment of a permanent fluidized region.[36] The presence of this fluidized region is evident from the expansion of the bed and the flattened free surface, which exhibits fluid-like behavior similar to that observed in a fluidized bed. It remains, however, unclear to what extent the flow behavior observed in a rotating drum can be linked to the fluidization behavior in unassisted and assisted fluidized beds.

In this work, we study the fluidization and flow properties of a range of commercially available cohesive powders with the objective of finding to what extent they are correlated. In the first part of the present work, the flowability properties are studied by employing a rotating drum powder flow analysis instrument. By performing measurements at different drum rotation speeds, we elucidate how the flow behavior of the various powders is influenced by the rotation speed. The second part of the present work presents an analysis of the fluidization properties in the absence and presence of mechanical vibration. We show that conventional methods to monitor the fluidization quality, namely total pressure drop and bed height, have significant shortcomings for cohesive powders. Instead, we argue that the directly observed flow pattern better represents the fluidization quality, and therefore, an advanced method that quantifies the fluidization quality based on the observed flow pattern is introduced in this work. The final part of this work consists of a detailed cross-comparison of the flow and fluidization properties to assess their inherent correlation. We argue that a good correlation implies that data obtained through flowability studies in a user-friendly rotating drum instrument could quickly and reliably indicate whether a certain cohesive powder is likely to be fluidized, with or without the implementation of an assistance method. Such insights hold promise for enhancing fluidization studies by providing a more efficient and reliable means of predicting powder fluidization behavior, thereby potentially optimizing fluidization processes.

2 | METHODOLOGY

2.1 | Materials

Ten commercially available materials were evaluated for their flowability and fluidization behavior. These materials included polystyrene,

15475905, 0, Downloaded from https://aiche.onlinelibrary.wiley.com/doi/10.1002/aic.18706 by Tu Delft, Wiley Online Library on [23/01/2025]. See the Terms and Conditions (https://onlinelibrary.wiley.com/terms-and-conditions) on Wiley Online Library for rules of use; OA articles are governed by the applicable Creative Commons License

egg white, bentonite, silica, lactose, four types of starches, and sorbitol. Sorbitol, a non-cohesive poly alcohol, was chosen as a reference material due to its excellent flowability. The particle size and morphology of the powders were analyzed using a particle size analyzer and scanning electron microscopy, respectively. The physical properties of the materials are summarized in Table 1 and will be further discussed in the following paragraphs.

The particle size distribution was measured using the Malvern 3000 particle size analyzer, equipped with a dry powder module and high-energy stainless steel venturi tube. Measurements were taken in an obscure range of 0.5%–8.0%. The volume-based particle size distributions of the materials are represented in Figure 1 by depicting respective d_{v10}, d_{v50}, and d_{v90} values. It can be observed that the d_{v50} ranges from 5.0 (Lactose) to 190 µm (Sorbitol), illustrating a significant spread in particle size across the materials studied. Based on their median (d_{v50}), volume-weighted mean ($d_{4,3}$), and area-weighted mean particle size ($d_{3,2}$), all powders can be classified as Geldart C type, except sorbitol, which is classified as a Geldart A type. However, as commonly encountered in real applications, the powders consist of a collection of particles that display a distribution in particle sizes. The width of the particle size distribution is quantified by computing the span as $(d_{v90} - d_{v10}/d_{v50})$. It can be observed that corn starch, tapioca starch, and polystyrene have a small span value, indicating a narrow particle size distribution. On the contrary, modified corn starch, bentonite, and egg white have a large span value, representing a wide particle size distribution.

The morphology of the powders was analyzed employing a JEOL JSM 7500F field emission scanning electron microscope with an acceleration voltage of 5 kV. The imaging was performed at magnifications between 100 and 1000. Before imaging, the samples were sputter-coated with gold to reduce sample charging and improve the image quality using a JEOL JFC-1300 auto fine coater in automatic mode for a gold sputtering duration of 30 s. Typical acquired scanning electron microscope images of the powders are depicted in Figure 2.

In agreement with the measured particle size shown in Figure 1, it can be observed that the powders display a significant spread in particle sizes (see Figure S1 for particle size distribution in the Supplementary Material S1). Moreover, notable differences are observed considering the morphology of the particles. On the one hand, potato starch, polystyrene, egg white, tapioca starch, and corn starch display a spherical shape with relatively smooth surfaces. On the other hand, sorbitol, modified corn starch, bentonite, silica, and lactose are characterized by an angular shape.

2.2 | Flowability experiments

2.2.1 | Rotating drum setup

The flowability of the materials was analyzed using the GranuDrum® rotating drum instrument.[33] This automated powder flowability analysis instrument is designed to characterize the flowability of materials in the dynamic flowing regime. The GranuDrum® comprises a rotating drum cylinder, an LED panel inducing contrast between powder and air, and a digital camera (5MP Monochrome CMOS). These components are positioned

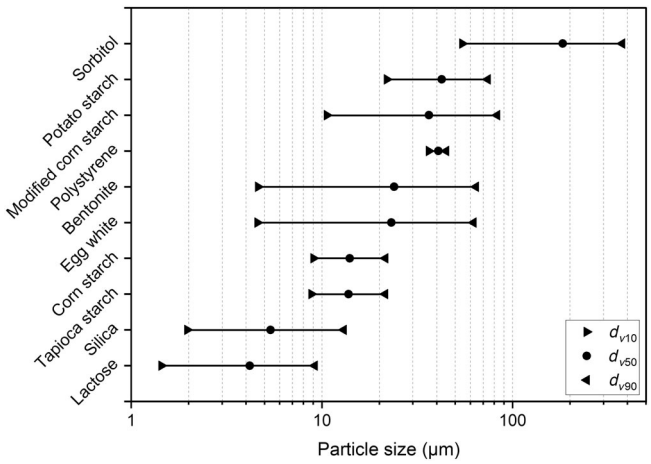

FIGURE 1 Volume-based particle size distribution of the powders included in this study.

TABLE 1 Physical properties of the powders used in this study.

Powder	$d_{4,3}$[a] (µm)	$d_{3,2}$[b] (µm)	Span[c] (–)	Shape	Geldart group[7]
Sorbitol	201.0	74.5	1.75	Angular	A
Potato starch	45.5	36.1	1.23	Spherical	C
Modified corn starch	42.3	19.4	1.98	Angular	C
Polystyrene	40.6	40.4	0.21	Spherical	C
Bentonite	29.8	10.3	2.49	Angular	C
Egg white	28.9	9.6	2.50	Spherical	C
Corn starch	14.7	13.2	0.89	Spherical	C
Tapioca starch	14.6	13.0	0.91	Spherical	C
Silica	6.6	4.1	2.05	Angular	C
Lactose	5.1	2.1	1.84	Angular	C

[a]Volume-weighted mean particle size.
[b]Area-weighted mean particle size.
[c]$(\text{Span} = d_{v90} - d_{v10}/d_{v50})$.

15475905, 0, Downloaded from https://aiche.onlinelibrary.wiley.com/doi/10.1002/aic.18706 by Tu Delft, Wiley Online Library on [23/01/2025]. See the Terms and Conditions (https://onlinelibrary.wiley.com/terms-and-conditions) on Wiley Online Library for rules of use; OA articles are governed by the applicable Creative Commons License

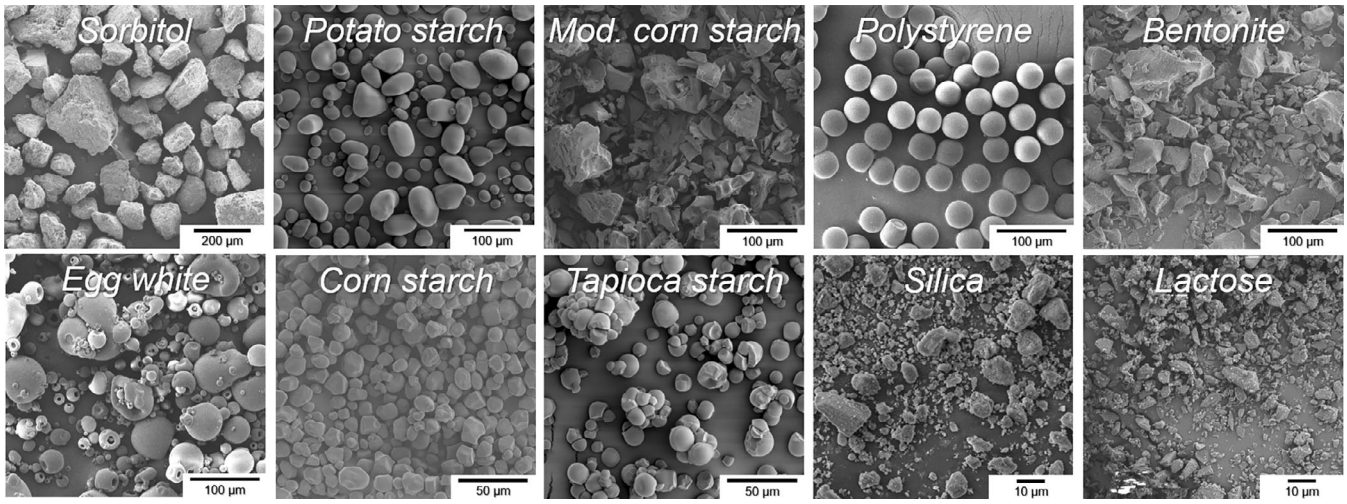

FIGURE 2 Scanning electron microscope images of the powders. It should be noted that images are acquired at magnifications between 100 and 1000. Therefore, the lengths of the scale bars presented in the respective images differ.

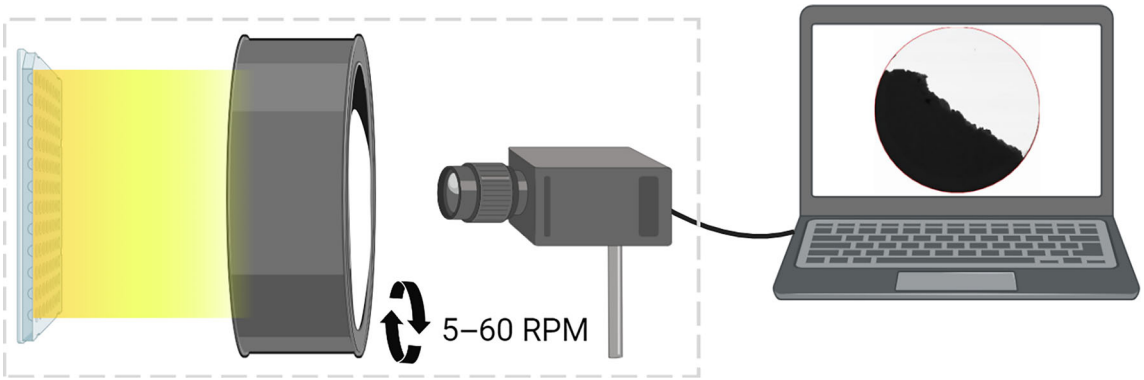

FIGURE 3 Schematic representation of the rotating drum setup. The GranuDrum® instrument consists of a rotating drum, digital camera, and LED panel. The instrument is connected to a computer for operation and image acquisition.

within a case to maintain consistent light conditions, as illustrated in Figure 3. The drum cylinder is made of stainless steel with sidewalls of transparent coated glass to allow visualization of the powder bed. The drum has an inner diameter of 84 mm and a depth of 20 mm, corresponding to a total volume of 110 mL. The depth of the drum significantly exceeds 6.4 times the mean particle radius (r) of all powders, such that front and back wall friction effects on the flow characteristics are mitigated according to Jain et al.[40] The instrument was connected to a computer for operation and image acquisition. The environmental temperature was maintained at 20°C, with humidity in a range of 30%–50%.

2.2.2 | Image acquisition and analysis

For each experiment, a volume of 55 cm^3 of the designated material was loaded in the drum cylinder, resulting in a 50% fill level. The drum was then placed in the instrument and rotated around its horizontal axis at rotation speeds of 5, 10, 30, and 60 RPM. The rotation speed was varied to elucidate how bed expansion, as the result of high angular velocities, influenced the flowability of the materials. At each rotation speed, the digital camera acquired a snapshot every 600 ms for a duration of 60 s, giving a total of 100 images. The camera was operated at a shutter speed of 0.85 ms to capture the bed dynamics at high rotation speeds accurately.

The acquired images were processed through a digital image analysis workflow introduced by Neveu et al.,[34] illustrated in Figure 4. For each image, the interface between the powder and air in the raw image (Figure 4a) was detected by an edge detection algorithm (Figure 4b). Subsequently, the detected powder surface is extracted (Figure 4c). This procedure is executed for all the images acquired during a measurement. From the extracted powder surface positions, a mean powder surface position and standard deviation are computed (Figure 4d) through Equation (1)[34]:

$$\sigma(x) = \sqrt{\frac{\sum_{i=1}^{N_y(x)} (\bar{y}(x) - y_i(x))^2}{N_y(x)}}, \quad (1)$$

15475905, 0, Downloaded from https://aiche.onlinelibrary.wiley.com/doi/10.1002/aic.18706 by Tu Delft, Wiley Online Library on [23/01/2025]. See the Terms and Conditions (https://onlinelibrary.wiley.com/terms-and-conditions) on Wiley Online Library for rules of use; OA articles are governed by the applicable Creative Commons License

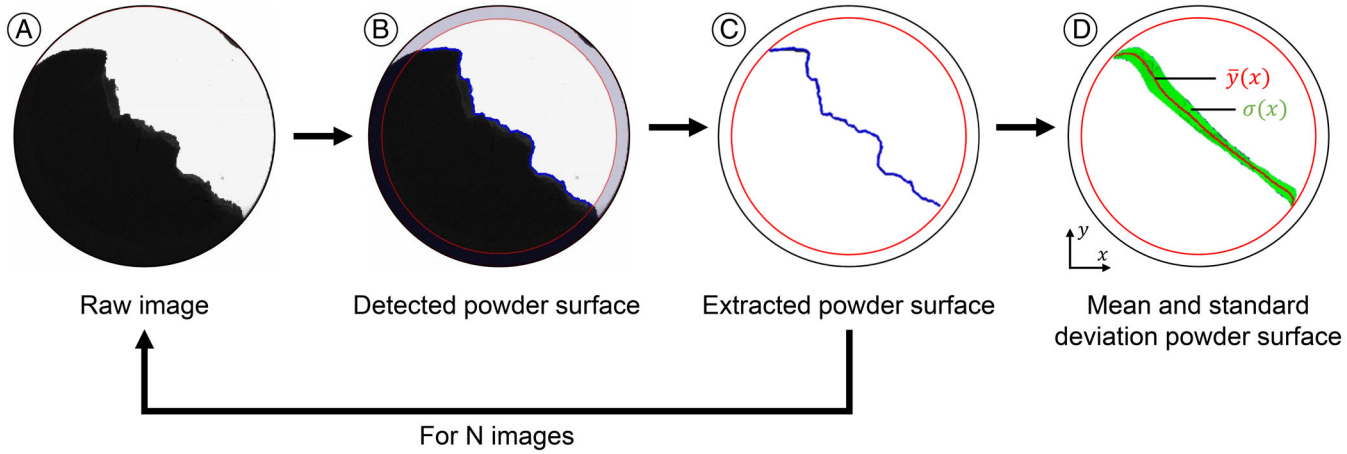

FIGURE 4 Image processing workflow to compute the cohesive index.

where $\sigma(x)$ is the standard deviation, $N_y(x)$ the number of images, $\bar{y}(x)$ the mean surface position, and $y_i(x)$ is the surface position for image i. The standard deviation of the surface position represents the temporal fluctuations of the powder surface and is correlated to the cohesive index (CI), a quantitative interpretable powder flowability descriptor, as:

$$\mathrm{CI} = \frac{1}{D_{\mathrm{crop}}} \sum_{x} \sigma(x), \tag{2}$$

where D_{crop} is the diameter of the cropped image.[41,42] The CI is related to powder flowability as depicted in Table 2. A low CI value, representing low temporal fluctuations of the powder surface, corresponds to excellent flowability, while a high CI value, representing significant temporal fluctuations of the powder surface, corresponds to poor flowability.[42]

TABLE 2 Classification of powder flowability based on the cohesive index.[42]

Flowability	Cohesive index
Excellent	<5
Good	≤5 < CI < 10
Fair	≤10 < CI < 20
Passable	≤20 < CI < 30
Poor	≤30 < CI < 40
Very poor	≤40 < CI < 50
Very, very poor	≥50

Abbreviation: CI, cohesive index.

2.3 | Fluidization experiments

Many challenges are associated with fluidizing cohesive powders, such as agglomeration, channeling, and plugging.[7] In this study, mechanical vertical vibration is employed as an assistance method to initiate or improve the fluidization of the powders. The influence of vertical vibration on the fluidization behavior of the powders was systematically assessed by evaluating the pressure drop, bed height, flow pattern, and gas holdup without mechanical vibration (referred to as unassisted fluidization) and with vertical vibration employed (referred to as vibro-assisted fluidization).

2.3.1 | Fluidized bed column

A laboratory-scale fluidized bed setup was used to assess the fluidization behavior of the powders. The fluidized bed column was comprised of a 50 mm inner-diameter perspex cylinder with a length of 400 mm coupled to a plenum-chamber beneath using a 3 mm thick sintered stainless steel distributor plate to allow even gas distribution. The distributor plate was cleaned using an ultrasound bath before use. For each experiment, a volume of 200 cm^3 of fresh powder was gently dosed and loaded into the column, corresponding to an initial bed height of 10 cm. This procedure was consistently followed to ensure comparable initial conditions for all experiments. An expansion breakout box was installed atop the column to recycle entrained powder. The gas vent was directed through a wash bottle and solids HEPA filter to collect escaped particles before releasing the fluidizing gas into the atmosphere. Compressed air, dried and filtered to remove oil and dust, was directed into the column through a mass flow controller (Bronkhorst F-202AV). The flow rate was set to achieve a superficial gas velocity of 6 cm s^{-1} at 20°C. This velocity is sufficiently high to fully fluidize Sorbitol powder, which has the highest theoretical minimum fluidization velocity (U_{mf}) among the powders studied. The column was mounted on a vibration table to facilitate vibro-assisted fluidization with vertical oscillation. In this study, the vibro-assisted fluidization experiments were performed through vertical vibration with a frequency of 30 Hz and an amplitude of 1 mm. This condition has been shown to effectively enhance fluidization of cohesive powders.[18]

15475905, 0, Downloaded from https://aiche.onlinelibrary.wiley.com/doi/10.1002/aic.18706 by Tu Delft, Wiley Online Library on [23/01/2025]. See the Terms and Conditions (https://onlinelibrary.wiley.com/terms-and-conditions) on Wiley Online Library for rules of use; OA articles are governed by the applicable Creative Commons License

2.3.2 | X-ray imaging method

The fluidization behavior of the various powders was experimentally assessed using an in-house fast X-ray imaging setup. X-ray imaging is a non-invasive imaging method that allows visualization of opaque multiphase flows. Through X-ray imaging, a 2D projection of the 3D gas holdup in the fluidized bed was captured. The X-ray setup consists of a standard industrial-type X-ray source (Yxlon International GmbH) with a maximum energy of 150 keV working in cone beam mode and a 2D detector (Teledyne Dalsa Xineos) with a theoretical spatial resolution of 0.15 mm placed opposite of the source. To ensure a safe working environment, the setup was controlled from a workstation located outside the setup room during the measurements. X-ray images were acquired at a sampling rate of 50 Hz over a measurement period of 120 s, equating to the acquisition of 6000 images per experiment. The obtained data were then stored for subsequent digital image analysis.

Each acquired image is a time-resolved projected 2D intensity map of the fluidized bed. A two-point calibration protocol was performed to compute a gas holdup from the measurement intensity. This requires two reference images: an image of the empty column and an image of the full column. The X-ray measurement principle is based on the attenuation of X-rays traveling in a straight line from an X-ray source to a detector while passing through matter. The transmission of a monochromatic beam of high-energy photons with initial intensity I_0 through matter of constant density is described by the Lambert–Beer law:

$$I(z) = I_0 \exp(-\mu z). \tag{3}$$

Here, $I(z)$ denotes the intensity measured at the detector, μ is the attenuation coefficient, and z is the material thickness. In cases of varying attenuation, the measured intensity is the integral effect of local attenuation with the local attenuation coefficient. By applying the Lambert–Beer law, the measurement gas holdup map was derived from the measurement intensity map using the empty and full reference as depicted in Figure 5. The normalized gas holdup ε_g was calculated as follows:

$$\varepsilon_g = \frac{\ln(I_{\text{measurement}}/I_{\text{full}})}{\ln(I_{\text{empty}}/I_{\text{full}})}. \tag{4}$$

It should be noted that the normalized gas holdup in this study ranges from 0 to 1, where 1 represents pure gas and 0 dense packing of solids. Warm colors in the gas holdup map correspond to low X-ray attenuation, indicating high gas concentrations. In contrast, cold colors represent high X-ray attenuation, indicating low gas concentrations. A detailed validation of the method is presented in the work by Wu et al.[13]

2.3.3 | Fluidization quality index

The acquired X-ray images provide a qualitative description of the fluidization behavior. To allow a direct quantitative comparison to the quantitative CI, we developed a method to quantify the fluidization quality based on the acquired X-ray images. With the gas holdup ε derived from X-ray imaging, a time-averaged gas holdup profile $\bar{\varepsilon}_g$ can be calculated as follows:

$$\bar{\varepsilon}_g(x,y) = \frac{1}{N_{\Delta t}} \sum_{t=t_0}^{t_0+\Delta t} \varepsilon_g(x,y,t), \tag{5}$$

where $N_{\Delta t}$ is the number of X-ray imaging frames between t_0 and $t_0 + \Delta t$, x is the horizontal pixel position, and y is the vertical pixel position.

Moreover, the standard deviation of the gas holdup serves as an indicator of the flow pattern's variability over time. This metric allows for the assessment of how dynamic the system is, providing valuable

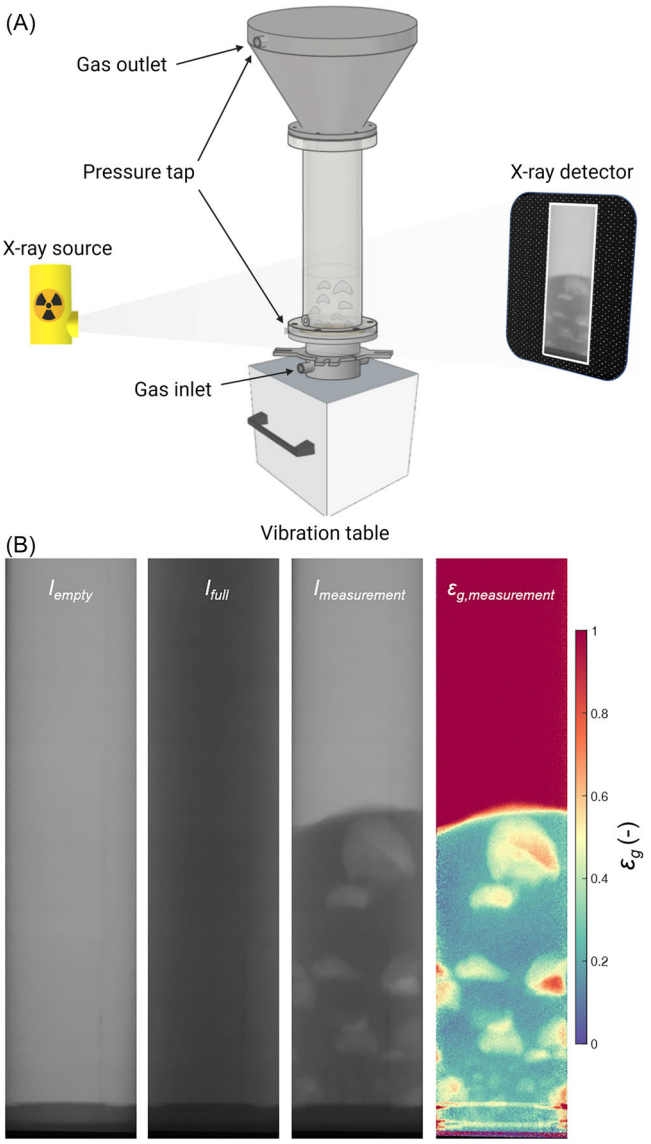

FIGURE 5 X-ray imaging analysis of the fluidized bed hydrodynamics: Schematic representation of the experimental setup (left), a two-point calibration procedure is employed to convert the intensity map to a gas holdup map (right).

15475905, 0, Downloaded from https://aiche.onlinelibrary.wiley.com/doi/10.1002/aic.18706 by Tu Delft, Wiley Online Library on [23/01/2025]. See the Terms and Conditions (https://onlinelibrary.wiley.com/terms-and-conditions) on Wiley Online Library for rules of use; OA articles are governed by the applicable Creative Commons License

insights into the flow patterns. For each pixel position (x,y) the time-based standard deviation of the gas holdup σ is computed as:

$$\sigma(x,y)=\sqrt{\frac{\sum_{t=t_0}^{t_0+\Delta t}[\varepsilon_g(x,y,t)-\bar{\varepsilon}_g(x,y)]^2}{N_{\Delta t}-1}}. \quad (6)$$

A low σ represents regions with less or no bubbling or other changes in density. On the contrary, regions with frequent bubbles and solid motion give rise to a large σ. Therefore, σ can be considered a quantitative indication of the system variability within a time interval.

Either the time-averaged gas holdup or its standard deviation solely cannot provide a fair quantitative description of the fluidization behavior. For instance, a channeling bed and a very homogeneously fluidized bed can exhibit similarly low standard deviation values. Furthermore, a bed of fine powder can have a loosely packed state with a high time-averaged gas holdup, yet is not possible to be fluidized. Therefore, incorporating both, we propose a quantitative description of the fluidization behavior that is the product of the time-averaged gas holdup and the temporal standard deviation of the domain-averaged gas holdup:

$$\mathrm{FQI}=\frac{1}{N_xN_y}\sum_{x=1}^{N_x}\sum_{y=1}^{N_y}[\bar{\varepsilon}_g(x,y)\times\sigma(x,y)]. \quad (7)$$

2.3.4 | Pressure analysis

Pressure drop measurements are commonly carried out in order to monitor and evaluate the fluidization quality. To assess the fluidization quality, the pressure drop across the powder bed was monitored with an OMEGA PX409-10WG5V differential pressure transducer. The gas pressure was probed at two positions: one located in the bed flange, ~6 mm above the distributor plate, and the other at the gas outlet of the bed. The pressure measurements were synchronized with the X-ray imaging system to ensure simultaneous data acquisition. The pressure drop was sampled at 1000 Hz, with a measurement error of 2% of the full scale (14 mbar), as specified by the manufacturer. The pressure drop across the bed was then obtained as the difference between the pressure measured at these two taps.

The evaluation of fluidization quality relies on the time-averaged pressure drop and the standard deviation of the pressure drop. The acquired pressure values (ΔP) were divided by the static pressure exerted by the powder, (ΔP_0), to yield a normalized pressure drop, a commonly used indicator of fluidization quality. Values of the normalized pressure drop correspond to the fraction of powder that is being fluidized.

$$\Delta P_0=\frac{mg}{A}, \quad (8)$$

where A is the column cross-sectional area, m is the mass of the powder and g is the gravitational acceleration.

2.3.5 | Bed expansion

The time-averaged bed height H is measured according to time-averaged gas fraction profiles obtained from X-ray imaging. The bed surface is identified based on the time-averaged series of radial-averaged gas fraction $\bar{\bar{\varepsilon}}_{g,y}$:

$$\bar{\bar{\varepsilon}}_{g,y}(y)=\frac{1}{N_xN_{\Delta t}}\sum_{t=t_0}^{t_0+\Delta t}\sum_{x=1}^{N}\varepsilon_g(x,y,t), \quad (9)$$

where $N_{\Delta t}$ is the number of X-ray imaging frames between t_0 and $t_0+\Delta t$, N_x is the number of pixel over the horizontal line at height y. The time-averaged bed height H is determined to height y where $\bar{\bar{\varepsilon}}_{g,y}$, counting from the freeboard to the bottom, first falls below 0.9. The bed expansion ratio H/H_0 is determined as the ratio of the time-averaged bed height H over the initial bed height H_0.

3 | RESULTS AND DISCUSSION

3.1 | Flow properties

3.1.1 | Flow pattern

The powder flowability was analyzed using the GranuDrum® rotating drum instrument for a range of rotation speeds varying from 5 to 60 RPM. Figure 6 depicts typical snapshots of the granular flow behavior for a rotation speed of 5, 10, 30, and 60 RPM. Notably, for free-flowing powders, such as sorbitol, the observed flow behavior is intrinsically linked to the drum rotation speed. As mentioned earlier, free-flowing powders transit through six flow modes upon an increasing rotation speed: slipping, slumping, rolling, cascading, and finally centrifuging.[43]

This behavior can be observed for sorbitol, which is free-flowing and non-cohesive, and depicts a flat surface at a rotation speed of 5 RPM, while cascading motion, characterized by an S-shape surface,[44] is observed when inertial effects become more pronounced at a rotation speed of 60 RPM. For all other powders, however, the cohesive nature gives rise to a more complex flow structure, as already observed by Rietema.[35] At a rotation speed of 5 RPM, the cohesive powders show intermittent quasiperiodic avalanches of lumps. The bed is characterized by large values of the dynamic angle of repose and rough powder surfaces due to the formation of lumps.

On the contrary, at a rotation speed of 60 RPM, four different types of behavior can be distinguished. The first behavior is cascading motion, characterized by an S-shape powder surface. As mentioned earlier, this behavior is typical for free-flowing powders when exposed to elevated rotation speeds, such as sorbitol in this study. The second type of flow behavior is associated with intermittent quasiperiodic avalanches, which is similar to the behavior most (mildly) cohesive powders display at low rotation speeds. This behavior is observed for the powders polystyrene, tapioca starch, and lactose, which continue to show intermittent quasiperiodic avalanche flow behavior similar to

15475905, 0, Downloaded from https://aiche.onlinelibrary.wiley.com/doi/10.1002/aic.18706 by Tu Delft, Wiley Online Library on [23/01/2025]. See the Terms and Conditions (https://onlinelibrary.wiley.com/terms-and-conditions) on Wiley Online Library for rules of use; OA articles are governed by the applicable Creative Commons License

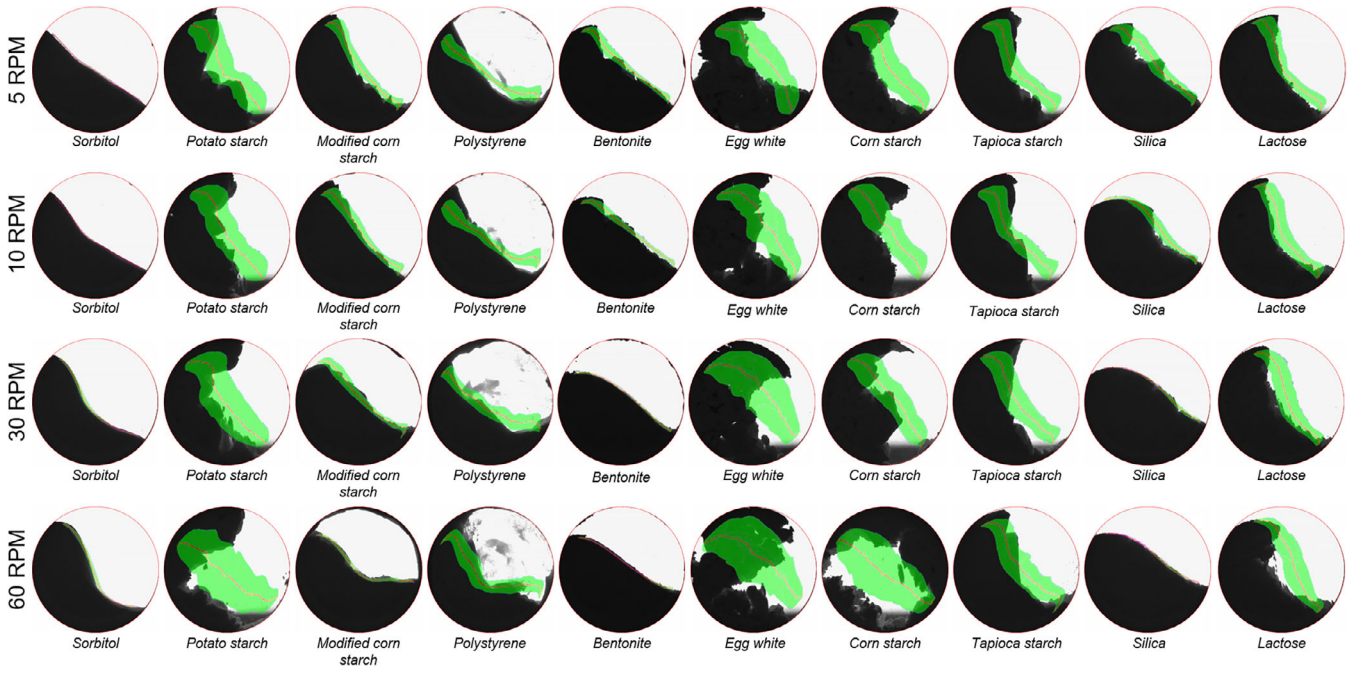

FIGURE 6 Representative snapshots of the flow pattern of the powders at rotation speeds of 5, 10, 30, and 60 RPM, ordered from top to bottom. The mean (red line) and standard deviation (green area) of the powder surface position are superimposed with transparency over the flow pattern images. Video S1 displaying the flow behavior is included in the electronic supplementary.

their respective 5 RPM behavior. A third type of flow behavior is distinguishable from its 5 RPM counterpart by a flattened, aerated powder bed, as ambient gas is entrained in the bulk due to the fast mixing. This results in an expanded state in which the free surface flattens.[37] Due to the aeration, the flowability of these powders is significantly improved. From Figure 6, it becomes evident that the powders modified corn starch, bentonite, and silica show this type of behavior. The observation that a bed of these powders is prone to become aerated is promising when considering their fluidization potential. Finally, the last type of behavior is associated with powder adherence to the walls of the drum. When subjected to high rotation speed, highly cohesive powders undergo frequent revolutions along the perimeter of the drum without displaying typical avalanche behavior. This type of behavior can be observed for potato starch, egg white, and corn starch. The irregular position of the powder surface also shows that the angle of repose would be inadequate in characterizing the flowability of powder of high cohesiveness.

3.1.2 | Cohesive index

While the flow pattern can give qualitative insight into the flowability of the powders, it is yet difficult to compare the flowability among different powders. Therefore, the flow behavior was quantified with the CI using a digital image analysis workflow. As mentioned earlier, the CI is a standardized quantitative interpretable powder flowability descriptor based on the temporal fluctuations of the powder surface. The mean and standard deviation of the powder surface position are superimposed with transparency over the flow pattern images in Figure 6. The CI is plotted against the rotation speed in Figure 7.

The powders identified with similar types of flow behavior can be further distinguished according to the CI. In line with the qualitative flow behavior, the free-flowing nature of sorbitol consequently results in a low CI for all tested rotation speeds. By referring to Table 2, the flowability can be classified as excellent too good. The powders modified corn starch, bentonite, and silica experienced significant aeration upon an increasing rotation speed, improving their flowability.[45] In agreement with the observed flow behavior, this is clearly observed by the downward trend in the CI for an increase in rotation speed. The flowability ranges from passable and poor at a rotation speed of 5 RPM to good and excellent at a rotation speed of 60 RPM. Polystyrene, tapioca starch, and lactose depict a higher CI and show a minor increase in the CI for an increase in rotation speed, indicating that their flowability is not significantly affected. Their flowability can be considered poor to very, very poor. Finally, potato starch, egg white, and corn starch depict an even higher CI and demonstrate a significant increase upon an increase in rotation speed. According to their CI, the flowability is classified as very, very poor. This is in agreement with the observed behavior, which was characterized by adherence to the walls of the drum. Interestingly, when relating the qualitative and quantitative flow behavior to the mean particle size, span, and shape of the powders (see Table 1), it becomes evident that there is no relation, underscoring the complexity associated with the flow of cohesive powders. Overall, the quantitative CI is found to be in good agreement with the qualitative description of the flow pattern.

15475905, 0, Downloaded from https://aiche.onlinelibrary.wiley.com/doi/10.1002/aic.18706 by Tu Delft, Wiley Online Library on [23/01/2025]. See the Terms and Conditions (https://onlinelibrary.wiley.com/terms-and-conditions) on Wiley Online Library for rules of use; OA articles are governed by the applicable Creative Commons License

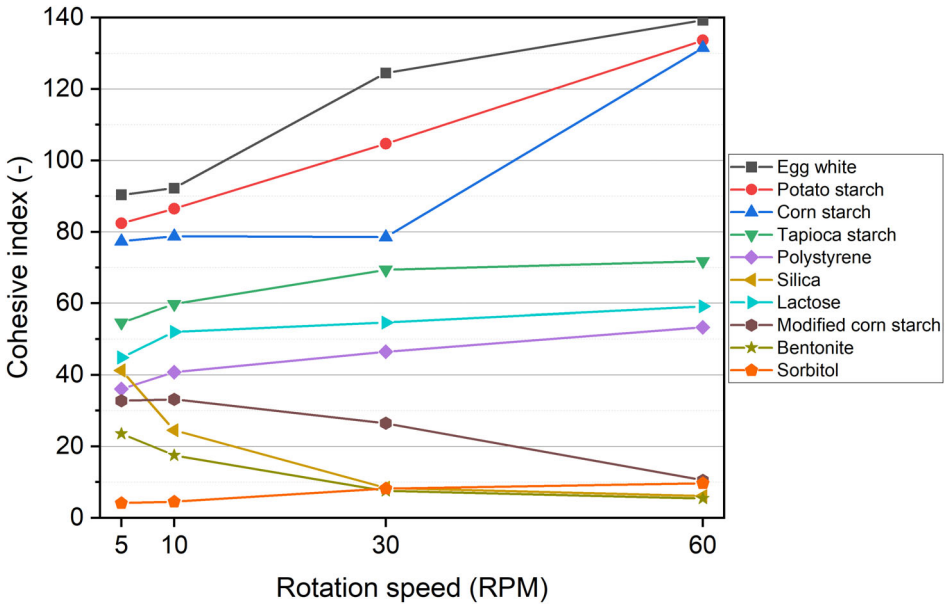

FIGURE 7 The flow behavior quantified by the cohesive index.

3.2 | Fluidization properties

3.2.1 | Flow pattern

Figure 8 demonstrates the comparison between the time-resolved flow patterns of unassisted and vibro-assisted fluidization. Without any external assistance, the intrinsic cohesiveness of most powders leads to the formation of gas channels of varying sizes, which allows the inlet gas to bypass the bed, thereby resulting in poor gas–solid interactions and a largely stationary bed. This effect is particularly pronounced in powders characterized by a high CI. Within this context, the nature of fluidization behavior is further distinguished by the morphology of the gas channels; for instance, potato starch, egg white, and tapioca starch exhibit the formation of curved macrochannels (also known as rat holes), whereas corn starch and lactose powder beds present branched micro-channels.

When comparing the flow patterns between unassisted and assisted fluidization, it becomes clear that the introduction of mechanical vibration generally modifies the dynamics of powder fluidization, especially in powders with high CIs, enhancing particle mobility significantly. It disrupts macro channels in modified corn starch, silica, and tapioca starch, although it is less effective against microchannels.[18] Notably, except for highly cohesive materials such as egg white, corn starch, potato starch, and lactose, other powders transition from micro-channeling fluidization behavior to a bubbling state, therefore remarkably enhancing fluidization. It should, however, be noted that potato starch displays fluidization of large agglomerates upon the introduction of mechanical vibration, as can be observed in Video S3 included in the electronic supplementary.

A comprehensive analysis of visual results allows for systematic categorization of fluidization behavior, ranging from a highly turbulent bubbling state to a relatively stationary sub-fluidized state. Figure 9 presents a comparison of the time-averaged flow patterns attained for unassisted fluidization and vibro-assisted fluidization. The time-averaged flow patterns demonstrate that powders prone to forming micro or macro channels tend to remain static (i.e., little difference between the pattern in Figures 8 and 9), leading to an uneven distribution of gas and solids, as illustrated in Figure 9. Additionally, the formation of gas-channeling structures is notably stable, while mechanical vibrations enhance the overall mobility of particles. However, it is observed that powders forming micro-channels still exhibit limited mobility, while those forming large channels or bubbles show a significantly improved homogeneity in gas–solids mixing.

3.2.2 | Bed expansion

Figure 10 compares the bed expansion in both unassisted and assisted beds across the various powder types. Notably, the application of mechanical vibrations contributes to an increased bed expansion, except for egg white and lactose powders. Bentonite displays the most significant bed expansion, approximately doubling its static height ($H/H_0 = 2$), which corresponds to the observed intensive bubbling fluidization behavior. Under vibration assistance, the fluidization of these powders is further enhanced, which is particularly notable with silica, tapioca, and potato starch powders, as the disruption of microchannels significantly elevates powder expansion. In contrast, for Geldart Group A Sorbitol powder, a high degree of fluidization was already attained in the absence of mechanical vibration. Therefore, the assistance did not add to any significant bed expansion. This indicates that, while vibration enhances bubbling behavior, that is creating more bubbles of small sizes, while it is not necessary to further enhance the dilation of emulsion phase. In addition, this level of bed expansion is not inherently superior to those powders under sub-

15475905, 0, Downloaded from https://aiche.onlinelibrary.wiley.com/doi/10.1002/aic.18706 by Tu Delft, Wiley Online Library on [23/01/2025]. See the Terms and Conditions (https://onlinelibrary.wiley.com/terms-and-conditions) on Wiley Online Library for rules of use; OA articles are governed by the applicable Creative Commons License

fluidized conditions, such as egg white and modified corn starch. Therefore, these results demonstrate that, due to the cohesive nature, a higher bed expansion is indicative of a fluidized state, while it cannot be used to compare across different powders to determine the fluidization quality directly. This finding aligns with our prior research as it suggests that an elevated bed expansion does not necessarily provide direct insights into the internal arrangement of powder particles.[18,19]

3.2.3 | Pressure analysis

Figure 11 shows the normalized pressure drop of the unassisted and vibro-assisted beds. It can be observed that the normalized pressure drop increases and becomes more stable upon the introduction of mechanical vibrations. In light of the X-ray images presented in Figures 8 and 9, the pressure drop graphs do, however, also highlight the shortcomings of using the total pressure drop as the sole indicator of fluidization quality, as pointed out in earlier work.[19] The normalized pressure drop only serves as a useful tool when the measured pressure drop indeed stems from fluidized particles, which is typically the case for non-cohesive powders. In contrast, the obtained pressure drop measured over beds of cohesive powders is potentially influenced by multiple phenomena, including spouting, plugging, arching, and fluidization.

Whereas the presence of one or more of these phenomena can be deduced from the otherwise nonphysical results of unassisted lactose and vibro-assisted fluidized egg white, as the normalized pressure drop exceeded unity, in the case of corn starch, the X-ray images demonstrate the presence of semi-stable structures in the bed. Normalized pressure drops are a strong

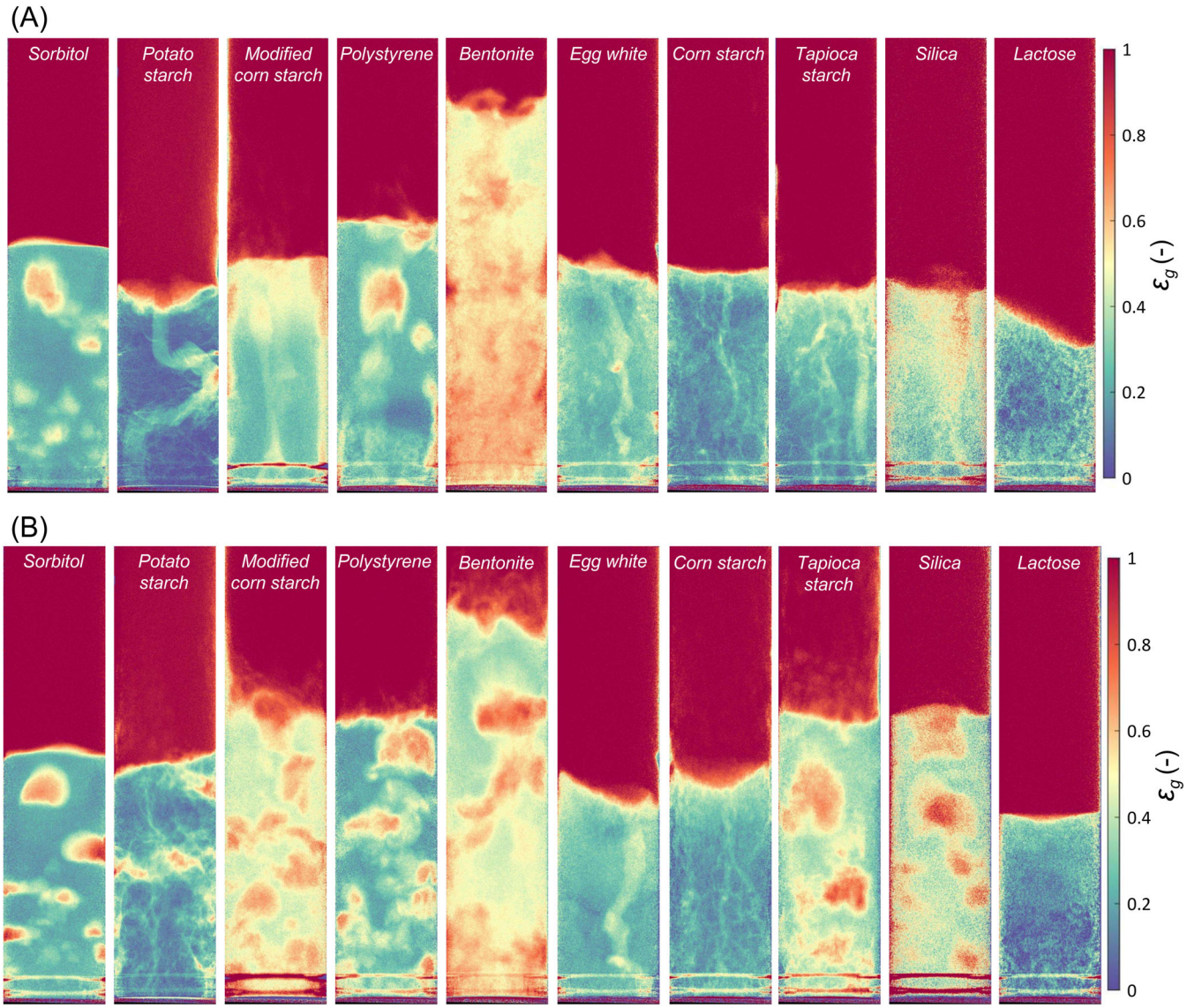

FIGURE 8 Representative still images of the flow patterns of the unassisted (top) and vibro-assisted beds (bottom). Videos S2 and S3 displaying the evolution of the flow patterns are included in the electronic supplementary.

15475905, 0, Downloaded from https://aiche.onlinelibrary.wiley.com/doi/10.1002/aic.18706 by Tu Delft, Wiley Online Library on [23/01/2025]. See the Terms and Conditions (https://onlinelibrary.wiley.com/terms-and-conditions) on Wiley Online Library for rules of use; OA articles are governed by the applicable Creative Commons License

indicator of fluidization quality for well-fluidizing powders (sorbitol, bentonite, silica), but on the boundary of Geldart group C and A, powders may experience channeling and plugging behavior, rendering the pressure data misleading if not interpreted with the utmost care.

3.2.4 | Fluidization quality index

Figure 12 illustrates the computed fluidization quality index (FQI) based on the flow patterns discussed on Flow_Pattern. By comparing FQI to the flow patterns shown in Figure 8, it is concluded that FQI can effectively classify different fluidization states, ranging from homogeneous bubbling and partial bubbling to micro- and macro-channeling (also known as rat-holes) to complete stationary, and is found to proportionally increases in this order. Such quantification is independent of the expanded bed height and highlights the dynamic elements in the bed, which is the key to evaluating fluidization behavior.

Generally, it is observed that FQI increases with the application of mechanical vibration, with notable exceptions such as lactose powder, which predominantly forms micro-channels. Significant improvements are found with tapioca, silica, and modified corn starch when the vibration is applied. Their flow patterns also show that existing channels have been disrupted, transitioning into a bubbling stage—a change quantitatively described by doubling the FQI. In comparison to the pressure drop and bed expansion ratio, FQI appears to be an effective indicator for describing the fluidization state of cohesive powders.

It becomes clear that the fluidization behavior cannot be simply governed by the mean particle size, size distribution span, and shape factor solely (see Table 1), but as a collective behavior of the particle properties. This underscores the limitations of traditional methods that aim to predict fluidization behavior.

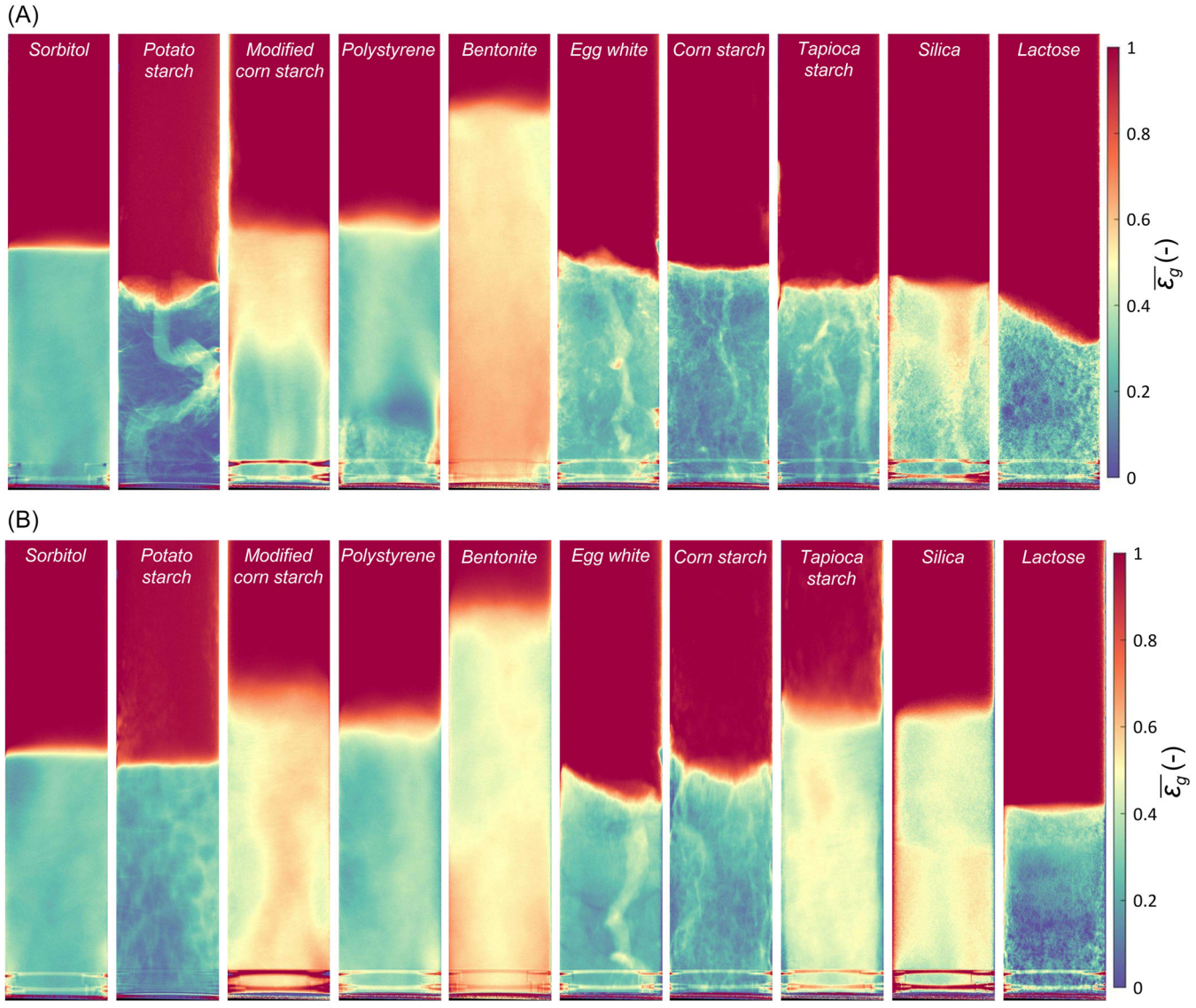

FIGURE 9 Time-averaged flow pattern of the unassisted (top) and vibro-assisted hydrodynamics (bottom).

15475905, 0, Downloaded from https://aiche.onlinelibrary.wiley.com/doi/10.1002/aic.18706 by Tu Delft, Wiley Online Library on [23/01/2025]. See the Terms and Conditions (https://onlinelibrary.wiley.com/terms-and-conditions) on Wiley Online Library for rules of use; OA articles are governed by the applicable Creative Commons License

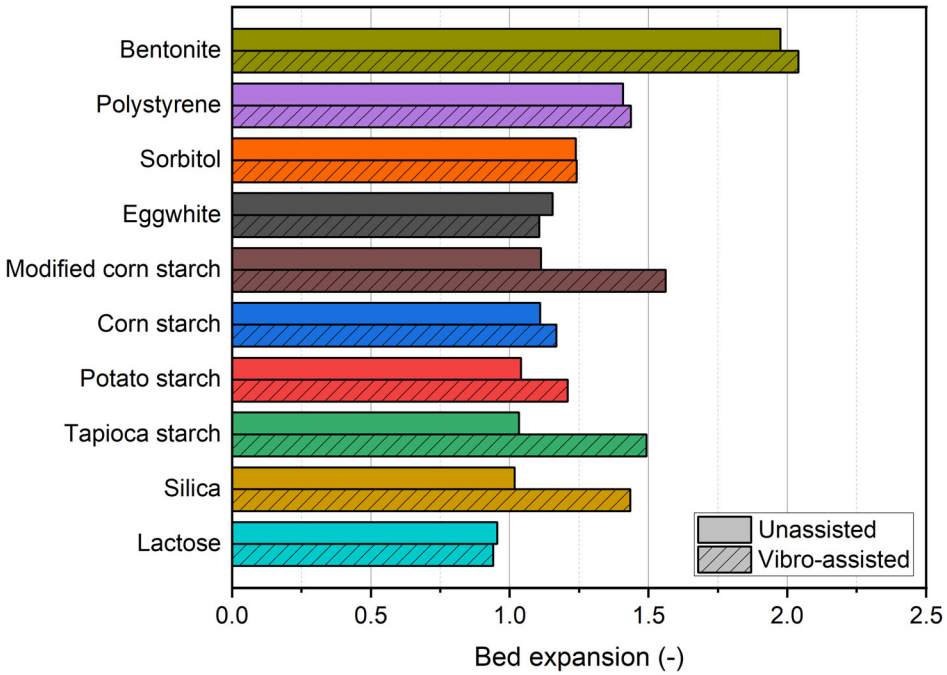

FIGURE 10 Time-averaged the bed expansion ratio. The expansion ratio is computed by dividing the time-averaged bed height (Figure 9) by the settled bed height.

3.3 | Comparison fluidization and flow property

The flowability characterization measurements demonstrated that the rotation speed has a significant impact on the apparent flowability of the powders. According to the literature mentioned above, when the rotation speed is high, such as the 60 RPM used in this study, the powder bed expands and achieves an aerated state comparable to that of a gas–solid fluidized bed. Therefore, the flow characteristics observed in an aerated state in a rotating drum instrument are likely correlated with the associated fluidization behavior.

As discussed above, unlike Geldart A and B particles, cohesive fine powder exhibits more complex and in-homogeneous flow patterns subjected to fluidization. It is evident that the normalized total pressure drop and bed expansion, which are commonly used to monitor fluidization quality for Geldart A and B particles, have limitations in accurately characterizing the fluidization quality of cohesive powders. As an alternative, the flow pattern-based FQI is adopted here to evaluate the observed fluidization behavior. The results show that the FQI quantifies and distinguishes various fluidization states, as given in Table 3.

By analyzing the flowability at different rotation speeds, we found that a flowability test with a rotation speed of 60 RPM is best correlated to the fluidization descriptor. A summary of the acquired flow and fluidization properties is presented in Table 3, where we provide the reciprocal of the FQI, denoted as FQI^{-1}, for ease of comparison with the CI. A low FQI^{-1} indicates good fluidization property, while a high FQI^{-1} indicates poor fluidization property. Specifically, powders with good and fair flowability (CI < 20) tend to exhibit bubbling or partial bubbling behavior during fluidization. An interesting observation is that this group includes bentonite, silica, and modified corn starch. These powders exhibited significant aeration and improved flowability as the rotation speed increased (see Figures 6 and S2). On the other hand, powders with very poor flowability (CI > 40) tend to demonstrate macro-channeling (also known as rate-hole) and static powder behavior. Moreover, for very cohesive powders in the regime of very, very poor flowability, the fluidization behavior can be further distinguished. The transition from micro-channeling (CI between 50 and 75) to macro-channeling (CI > 140) indicates that the fluidization phenomena are connected to quantitative measurements of the CI.

With the assistance of mechanical vibration, the fluidization quality can be improved for certain powders. The table indicates that powders with a CI lower than 75 are effectively facilitated, showing a transition from channeling to bubbling. For powders that originally exhibit bubbling behavior, mechanical vibration improves bubbling with the observation of an increased number of smaller bubbles in the bed and a lower FQI^{-1} value, indicating higher gas holdup and/or more intense gas–solids mixing. Powders with a CI higher than 75 (specifically corn starch, potato starch, and egg white) show some improvement with the assistance of mechanical vibration. However, it is evident that these powders cannot be fluidized under these conditions, despite corn starch and potato starch transitioning from rat-hole to channeling.

To visualize the relation, the FQI^{-1} is plotted against the CI in Figure 13. In accordance with the above, powders with a high CI value (tapioca starch, egg white, potato starch, and corn starch) display a high FQI^{-1} value. Conversely, powders with a low CI value (silica, bentonite, sorbitol) display a low FQI^{-1} value. Although the data is loosely scattered, a positive correlation between the CI and the FQI^{-1} is clearly observed, further supporting the intrinsic connection between the flowability and

15475905, 0, Downloaded from https://aiche.onlinelibrary.wiley.com/doi/10.1002/aic.18706 by Tu Delft, Wiley Online Library on [23/01/2025]. See the Terms and Conditions (https://onlinelibrary.wiley.com/terms-and-conditions) on Wiley Online Library for rules of use; OA articles are governed by the applicable Creative Commons License

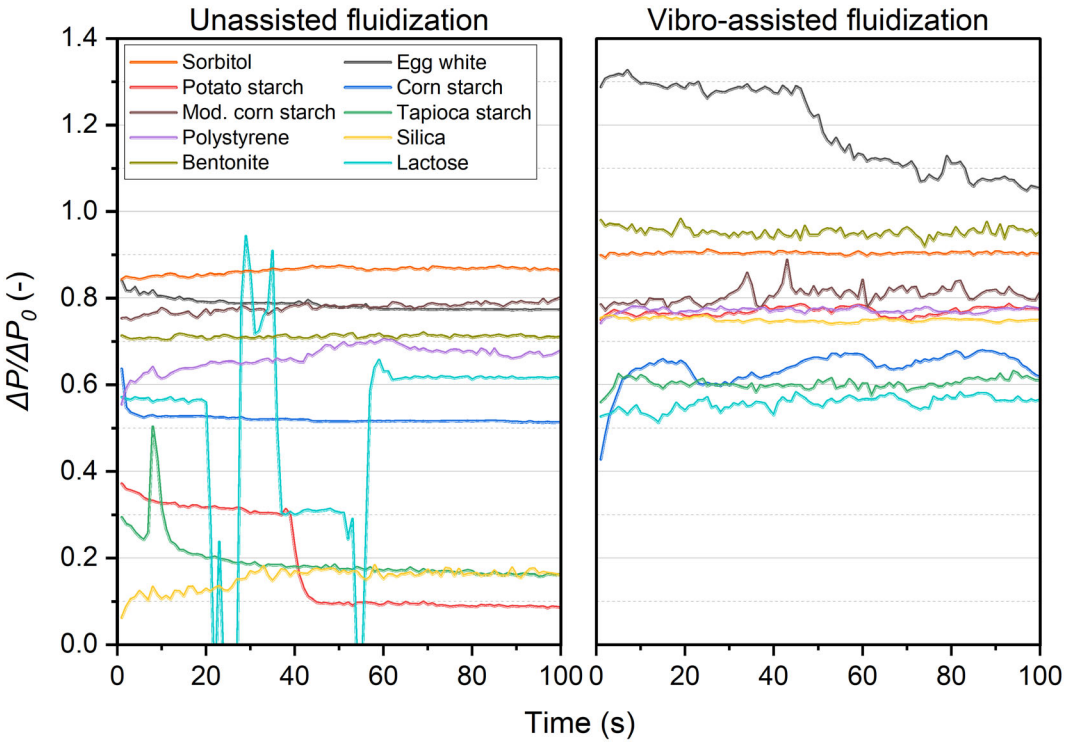

FIGURE 11 Temporal evaluation of the normalized pressure drop for unassisted fluidization (left) and vibro-assisted fluidization (right).

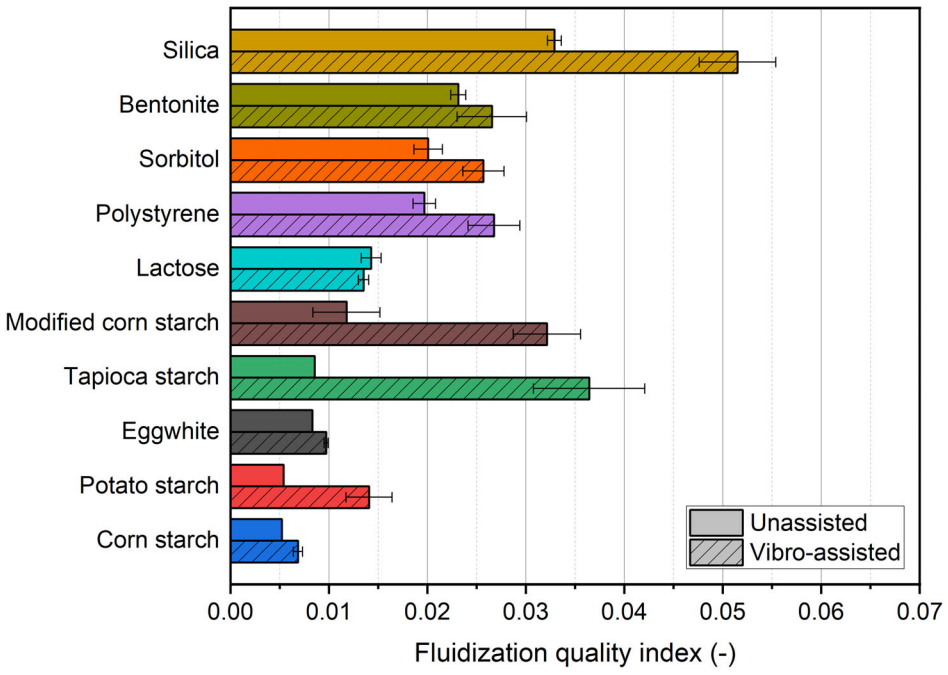

FIGURE 12 The fluidization behavior quantified by the fluidization quality index.

fluidization property. In addition, the designated CI value is shown to be capable of predicting the corresponding fluidization behavior of the cohesive powders. When comparing unassisted fluidization with vibro-assisted fluidization, it is evident that mechanical vibration leads to a decrease in the FQI^{-1} across all powder types, indicating an improvement in fluidization quality. However, the powders with a CI exceeding 100 are still challenging to be fluidized, even with vibration assistance. This highlights the CI's potential as a predictive indicator of the associated fluidization quality in practical applications. Based on these observations, it is clear that flowability and fluidization properties are inherently correlated.

15475905, 0, Downloaded from https://aiche.onlinelibrary.wiley.com/doi/10.1002/aic.18706 by Tu Delft, Wiley Online Library on [23/01/2025]. See the Terms and Conditions (https://onlinelibrary.wiley.com/terms-and-conditions) on Wiley Online Library for rules of use; OA articles are governed by the applicable Creative Commons License

TABLE 3 Comparison fluidization and flow property.

Powder	Flow descriptor (CI)[a] 60 RPM	Fluidization descriptor (FQI^{-1}) Unassisted	Fluidization descriptor (FQI^{-1}) Vibro-assisted
Bentonite	Good (5.5)	Bubbling (43.2)	Bubbling (37.7)
Silica	Good (6.1)	Mild bubbling (30.4)	Bubbling (19.4)
Sorbitol	Good (9.7)	Bubbling (49.8)	Bubbling (38.9)
Modified corn starch	Fair (10.5)	Mild bubbling (84.9)	Bubbling (31.1)
Polystyrene	Very, very poor (53.4)	Mild bubbling (50.8)	Bubbling (37.4)
Lactose	Very, very poor (59.2)	Channeling (70.0)	Mild bubbling (74.0)
Tapioca starch	Very, very poor (71.8)	Channeling (116.8)	Bubbling (27.4)
Corn starch	Very, very poor (131.5)	Rat-hole (191.9)	Channeling (146.0)
Potato starch	Very, very poor (133.6)	Rat-hole (185.2)	Channeling (71.1)
Egg white	Very, very poor (139.3)	Rat-hole (120.2)	Rat-hole (103.0)

Abbreviations: CI, cohesive index; FQI, fluidization quality index.
[a]As measured at a rotation speed of 60 RPM.

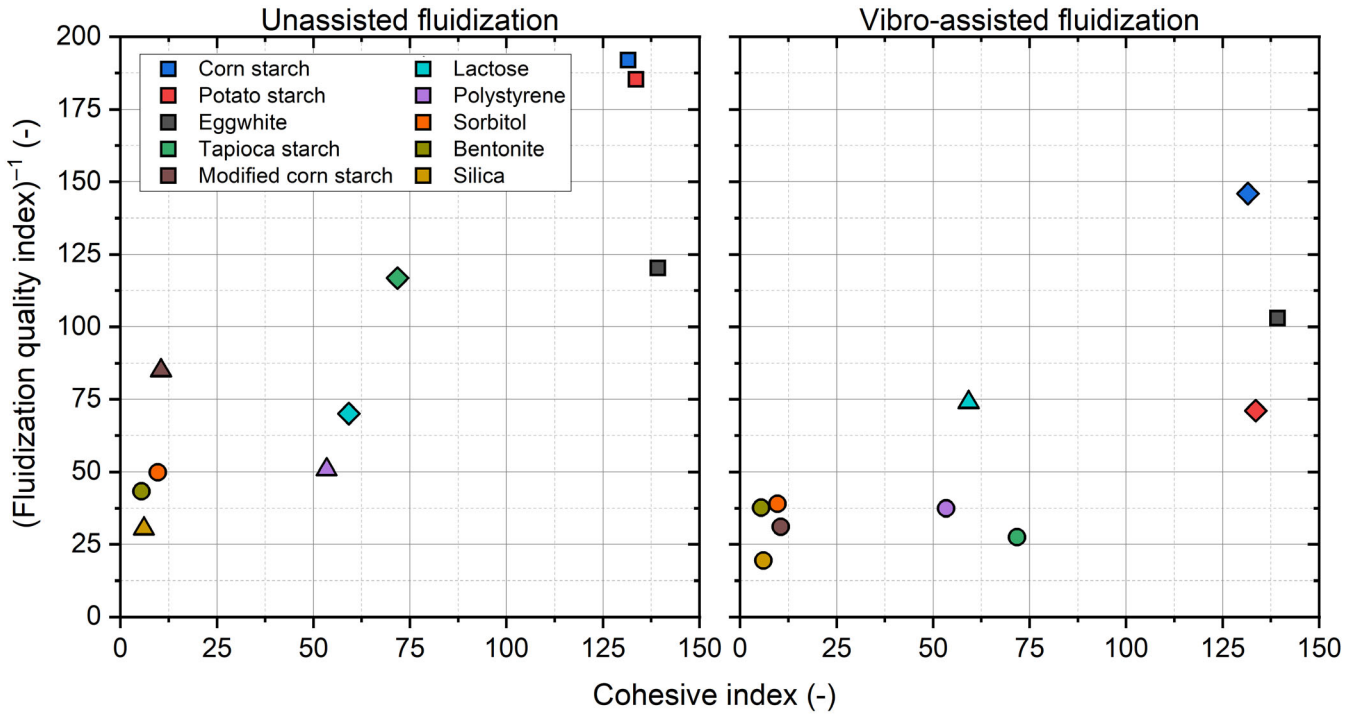

FIGURE 13 Cohesive index against the reciprocal of the fluidization quality index for unassisted fluidization (left) and vibro-assisted fluidization (right). The cohesive index values are measured at a rotation speed of 60 RPM. The symbols correspond to the qualitative fluidization descriptor: Rat-hole □, channeling ◇, mild bubbling Δ, and bubbling ○.

4 | CONCLUSIONS

In this study, a comprehensive examination of the fluidization and flow properties of 10 commercially available materials was conducted through rotating drum and fluidization experiments. Operating the rotating drum instrument at a rotation speed of 60 RPM generates an aerated state within the powder bed, which allows for comparable flow field and stress conditions as in a fluidized bed. By analyzing the fluidization behavior, it was observed that widely applied analyses based on normalized pressure drop and bed expansion, which are typically used for assessing the fluidization quality of Geldart A and B powders, have limitations when applied to cohesive powders. Therefore, the fluidization behavior was quantified based on the observed flow pattern, which was studied using X-ray imaging. A novel FQI was introduced, which combines the time-averaged gas holdup and the temporal standard deviation of the domain-averaged gas holdup, thereby offering a reliable indicator of fluidization quality.

15475905, 0, Downloaded from https://aiche.onlinelibrary.wiley.com/doi/10.1002/aic.18706 by Tu Delft, Wiley Online Library on [23/01/2025]. See the Terms and Conditions (https://onlinelibrary.wiley.com/terms-and-conditions) on Wiley Online Library for rules of use; OA articles are governed by the applicable Creative Commons License

By carefully comparing powder flowability and fluidization properties, a positive correlation between flowability (quantified by the CI) and fluidization quality (quantified by the inverse of the FQI) was established, underscoring their inherent relationship. This finding holds significance as it indicates that simple flowability measurements conducted in a rotating drum instrument can provide valuable insights into the expected fluidization quality of cohesive powders. Consequently, these insights offer a reliable means of predicting whether a cohesive powder is likely to fluidize, with or without assistance methods applied. This understanding holds promise for enhancing fluidization studies and optimizing industrial processes reliant on fluidization techniques.

AUTHOR CONTRIBUTIONS

P. Christian van der Sande: Conceptualization(supporting), methodology(lead); validation (lead); formal analysis (lead); investigation (lead); data curation (equal); writing—original draft (equal); visualization (lead). **Kaiqiao Wu:** Conceptualization (lead); methodology (lead); validation (supporting); formal analysis (supporting); investigation (supporting); data curation (supporting); writing—original draft (equal); visualization (supporting). **Rens Kamphorst:** Methodology (supporting); investigation (supporting); data curation (supporting), writing—original draft (equal). **Evert C. Wagner:** Investigation (supporting), writing—review editing (supporting). **Gabrie M. H. Meesters:** Project administration (supporting), writing—review editing (supporting), supervision (supporting). **J. Ruud van Ommen:** Conceptualization (supporting); project administration (lead); writing—review editing (lead); supervision (lead).

ACKNOWLEDGMENTS

The authors would like to acknowledge Granutools for the collaboration and for making available the GranuDrum® instrument in which the flowability experiments were performed. Moreover, they thank Stefan ten Hagen and Duco Bosma for the development of the fluidized bed column and for acquiring the SEM images, respectively. Finally, they acknowledge Emma Brockhus and Wietse Saalmink for their contributions to the experimental work. This work was carried out as part of the "Industrial Dense Granular Flows" project, which received funding from the Dutch Research Council (NWO) in the framework of the ENW PPP Fund for the top-sectors and from the Ministry of Economic Affairs in the framework of the "PPS-Toeslagregeling." This work was also supported by the National Natural Science Foundation of China (52406181).

CONFLICT OF INTEREST STATEMENT

The authors declare no conflicts of interest.

DATA AVAILABILITY STATEMENT

The data underlying Figures 1, 7, 10, 12, and 13 have been shared in the Supplementary Materials S1. Additional data that support the findings of this study are available from the corresponding author upon request.

ORCID

Kaiqiao Wu https://orcid.org/0009-0008-5561-1622

REFERENCES

1. Feng L, Liu Z. Graphene in biomedicine: opportunities and challenges. *Nanomedicine*. 2011;6:317-324.
2. Qu L, Liu Y, Baek JB, Dai L. Nitrogen-doped graphene as efficient metal-free electrocatalyst for oxygen reduction in fuel cells. *ACS Nano*. 2010;4(3):1321-1326.
3. Zhu X, Zhang Q, Huang C, Wang Y, Yang C, Wei F. Validation of surface coating with nanoparticles to improve the flowability of fine cohesive powders. *Particuology*. 2017;30:53-61.
4. Kamphorst R, Wu K, Salameh S, Meesters GMH, van Ommen JR. On the fluidization of cohesive powders: differences and similarities between micro- and nano-sized particle gas-solid fluidization. *Can J Chem Eng*. 2023;101(1):227-243.
5. Fan LS, Zhu C. *Principles of Gas-Solid Flows*. Cambridge University Press; 1998.
6. LaMarche WCQ, Liu P, Kellogg KM, Lattanzi AM, Hrenya CM. Toward general regime maps for cohesive-particle flows: force versus energy-based descriptions and relevant dimensionless groups. *AIChE J*. 2021;67(9):e17337.
7. Geldart D. Types of gas fluidization. *Powder Technol*. 1973;7(5):285-292.
8. Teleki A, Wengeler R, Wengeler L, Nirschl H, Pratsinis S. Distinguishing between aggregates and agglomerates of flame made TiO_2 by high-pressure dispersion. *Powder Technol*. 2008;181(3):292-300.
9. Niu L, Chu Z, Cai M, Liu M. Modified force balance model of estimating agglomerate sizes in a gas-solid fluidized bed. *Ind Eng Chem Res*. 2019;58(19):8472-8483.
10. Motlagh AA, Grace JR, Salcudean M, Hrenya C. New structure-based model for Eulerian simulation of hydrodynamics in gas–solid fluidized beds of Geldart group A particles. *Chem Eng Sci*. 2014;120:22-36.
11. Kamphorst R, van der Sande PC, Wu K, et al. The mechanism behind vibration assisted fluidization of cohesivemicro-silica. *KONA Powder Particle J*. 2024;41:254-264.
12. Alavi S, Caussat B. Experimental study on fluidization of micronic powders. *Powder Technol*. 2005;157(1):114-120.
13. Wu K, Kamphorst R, Bakker A, et al. Stirrer design for improving fluidization of cohesive powder: a time-resolved X-ray study. *Chem Eng Sci*. 2024;294:120069.
14. Al-Ghurabi E, Shahabuddin M, Siva Kumar N, Asif M. Deagglomeration of ultrafine hydrophilic nanopowder using low frequency pulsed fluidization. *Nanomaterials*. 2020;10:388.
15. Ali S, AL-Ghurabi E, Ajbar A, Mohammed Y, Boumaza M, Asif M. Effect of frequency on pulsed fluidized beds of ultrafine powders. *J Nanomater*. 2016;2016:1-12.
16. Chirone R, Raganati F, Ammendola P, Barletta D, Lettieri P, Poletto M. A comparison between interparticle forces estimated with direct powder shear testing and with sound assisted fluidization. *Powder Technol*. 2018;323:1-7.
17. Ammendola P, Chirone R. Aeration and mixing behaviours of nano-sized powders under sound vibration. *Powder Technol*. 2010;201(1):49-56.
18. Wu K, Wagner E, Ochkin-Koenig O, et al. Time-resolved X-ray study of assisted fluidization of cohesive micron powder: on the role of mechanical vibration. *Chem Eng J*. 2023;470:143936.
19. Kamphorst R, Wu K, van Baarlen M, Meesters GM, van Ommen JR. Effect of vibrational modes on fluidization characteristics and solid distribution of cohesive micro- and nano-silica powders. *Chem Eng Sci*. 2024;291:119911.
20. Carr RL. Evaluating flow properties of solids. *Chem Eng*. 1965;72(2):163-168.

15475905, 0, Downloaded from https://aiche.onlinelibrary.wiley.com/doi/10.1002/aic.18706 by Tu Delft, Wiley Online Library on [23/01/2025]. See the Terms and Conditions (https://onlinelibrary.wiley.com/terms-and-conditions) on Wiley Online Library for rules of use; OA articles are governed by the applicable Creative Commons License

21. Schwedes J. Review on testers for measuring flow properties of bulk solids. *Granul Matter*. 2003;5:1-43.
22. Thalberg K, Lindholm D, Axelsson A. Comparison of different flowability tests for powders for inhalation. *Powder Technol*. 2004;146(3):206-213.
23. Leturia M, Benali M, Lagarde S, Ronga I, Saleh K. Characterization of flow properties of cohesive powders: a comparative study of traditional and new testing methods. *Powder Technol*. 2014;253:406-423.
24. Ajabshir SZ, Barletta D, Poletto M. The effect of process conditions on powder flow properties for slow flow regimes. *KONA Powder Particle J*. 2024;2025006.
25. Mishra I, Molnar MJ, Hwang MY, Shetty A, Hrenya CM. Experimental validation of the extraction of a particle-particle cohesion model (square-force) from simple bulk measurements (defluidization in a rheometer). *Chem Eng Sci*. 2022;259:117782.
26. Krantz M, Zhang H, Zhu J. Characterization of powder flow: static and dynamic testing. *Powder Technol*. 2009;194(3):239-245.
27. Zhu L, Lu H, Poletto M, Liu H, Deng Z. Hopper discharge of cohesive powders using pulsated airflow. *AIChE J*. 2020;66(7):16240.
28. Mishra I, Liu P, Shetty A, Hrenya CM. On the use of a powder rheometer to probe defluidization of cohesive particles. *Chem Eng Sci*. 2020;214:115422.
29. Prescott JK, Barnum RA. On powder flowability. *Pharm Technol*. 2000;24(10):60.
30. Castellanos A, Valverde JM, Pérez AT, Ramos A, Watson PK. Flow regimes in fine cohesive powders. *Phys Rev Lett*. 1999;82(6):1156.
31. Liu XY, Specht E, Mellmann J. Experimental study of the lower and upper angles of repose of granular materials in rotating drums. *Powder Technol*. 2005;154(2-3):125-131.
32. Pirard SL, Lumay G, Vandewalle N, Pirard JP. Motion of carbon nanotubes in a rotating drum: the dynamic angle of repose and a bed behavior diagram. *Chem Eng J*. 2009;146(1):143-147.
33. Shi H, Lumay G, Luding S. Stretching the limits of dynamic and quasi-static flow testing on cohesive limestone powders. *Powder Technol*. 2020;367:183-191.
34. Neveu A, Francqui F, Lumay G. Measuring powder flow properties in a rotating drum. *Measurement*. 2022;200:111548.
35. Rietema K. *The Dynamics of Fine Powders*. Springer Dordrecht; 1991.
36. Castellanos A, Sanchez M, Valverde J. The onset of fluidization for fine powders in rotating drums. *Mater Phys Mech*. 2001;3:57-62.
37. Castellanos A, Valverde JM, Quintanilla MAS. Fine cohesive powders in rotating drums: transition from rigid-plastic flow to gas-fluidized regime. *Phys Rev E*. 2002;65:061301.
38. Huang Q, Zhang H, Zhu J. Experimental study on fluidization of fine powders in rotating drums with various wall friction and baffled rotating drums. *Chem Eng Sci*. 2009;64(9):2234-2244.
39. Huang Q, Zhang H, Zhu J. Onset of an innovative gasless fluidized bed-comparative study on the fluidization of fine powders in a rotating drum and a traditional fluidized bed. *Chem Eng Sci*. 2010;65(3):1261-1273.
40. Jain N, Ottino JM, Lueptow RM. Regimes of segregation and mixing in combined size and density granular systems: an experimental study. *Granul Matter*. 2005;7(2):69-81.
41. Orefice L, Remmelgas J, Neveu A, Francqui F, Khinast JG. A novel methodology for data analysis of dynamic angle of repose tests and powder flow classification. *Powder Technol*. 2024;435:119425.
42. Tondare VN, Whiting JG, Pintar AL, Moylan SP, Neveu A, Francqui F. An interlaboratory study for assessing repeatability and reproducibility of the data generated by rotating drum powder rheometers (part 1: Granudrum). *Powder Technol*. 2024;441:119810.
43. Henein H, Brimacombe JK, Watkinson AP. Experimental study of transverse bed motion in rotary kilns. *Metall Trans B*. 1983;14(2):191-205.
44. Taberlet N, Richard P, John HE. S shape of a granular pile in a rotating drum. *Phys Rev E*. 2006;73:050301.
45. Freeman R. Powder testing – dealing with the daily challenges. *Powder Handling Process*. 2005;17(5):294-296.

SUPPORTING INFORMATION

Additional supporting information can be found online in the Supporting Information section at the end of this article.

How to cite this article: van der Sande PC, Wu K, Kamphorst R, Wagner EC, Meesters GMH, van Ommen JR. On the inherent correlation between the fluidization and flow properties of cohesive powders. *AIChE J*. 2024;e18706. doi:10.1002/aic.18706

15475905, 0, Downloaded from https://aiche.onlinelibrary.wiley.com/doi/10.1002/aic.18706 by Tu Delft, Wiley Online Library on [23/01/2025]. See the Terms and Conditions (https://onlinelibrary.wiley.com/terms-and-conditions) on Wiley Online Library for rules of use; OA articles are governed by the applicable Creative Commons License